How to cite:
doi.org/10.1002/anie.202303117

CO_2 Reduction Hot Paper

Coordinating the Edge Defects of Bismuth with Sulfur for Enhanced CO_2 Electroreduction to Formate

*Lei Lv[+], Ruihu Lu[+], Jiexin Zhu[+], Ruohan Yu, Wei Zhang, Enhui Cui, Xingbao Chen, Yuhang Dai, Lianmeng Cui, Jiong Li, Liang Zhou, Wei Chen, Ziyun Wang, and Liqiang Mai**

Abstract: Bismuth-based materials have been recognized as promising catalysts for the electrocatalytic CO_2 reduction reaction (ECO_2RR). However, they show poor selectivity due to competing hydrogen evolution reaction (HER). In this study, we have developed an edge defect modulation strategy for Bi by coordinating the edge defects of bismuth (Bi) with sulfur, to promote ECO_2RR selectivity and inhibit the competing HER. The prepared catalysts demonstrate excellent product selectivity, with a high $HCOO^-$ Faraday efficiency of $\approx$95 % and an $HCOO^-$ partial current of $\approx$250 mA cm^{-2} under alkaline electrolytes. Density function theory calculations reveal that sulfur tends to bind to the Bi edge defects, reducing the coordination-unsaturated Bi sites (*H adsorption sites), and regulating the charge states of neighboring Bi sites to improve *OCHO adsorption. This work deepens our understanding of ECO_2RR mechanism on bismuth-based catalysts, guiding for the design of advanced ECO_2RR catalysts.

Introduction

The long-term reliance on fossil fuels has resulted in excessive carbon emissions, which have become a global concern.[1] It is important to lower the concentration of carbon dioxide (CO_2) through various technologies, such as electrocatalysis,[2] thermocatalysis,[3] photocatalysis,[4] and biocatalysis.[5] Electrocatalytic CO_2 reduction reaction (ECO_2RR) offers high catalytic efficiency, mild conditions, and controllability.[6] ECO_2RR uses intermittent electricity from wind and solar energy to convert CO_2 into various chemicals and fuels, offering one of the most promising methods for achieving carbon neutrality.[7]

Formic acid, a main product in ECO_2RR, is a high-energy-density molecule that can be easily stored and used for various applications such as fuel for formic acid fuel cells and as an intermediate for synthesizing of biopharmaceuticals and chemicals.[7] However, the competitive hydrogen evolution reaction (HER) in the aqueous electrolyte poses a challenge in achieving high selectivity of formic acid production using ECO_2RR.[8] Bi-based catalysts have shown the highest efficiency for formic acid conversion among various catalysts for ECO_2RR.[9] During ECO_2RR, Bi-based catalysts undergo reconstruction, and the valence state of Bi is reduced, making it difficult to identify the active sites of the catalysts. The coordination environment of Bi-based pre-catalyst has a significant influence on the morphology of reconstructed Bi, with most reconstructed catalysts having defects such as vacancies and steps.[10] For example, Bi_2S_3 nanowires are converted into vacancy-rich Bi nanosheets,[11] BiOBr nanosheets are converted into porous Bi nanosheets, and bismuth metal–organic framework is converted into ultra-thin Bi nanosheets with rich in-plane defects.[12] To improve ECO_2RR while reducing HER is key to developing effective Bi-based catalysts. From a chemical viewpoint, Bi defects with coordination unsaturated sites and exposed dangling bonds show high reactivity towards both ECO_2RR and HER intermediates, particularly hydrogen (*H) absorption. It is found that tailoring bulk Bi sites, such as strain and curvature, can deliver high catalytic activity towards ECO_2RR.[13] It indicates that activating bulk sites while passivating edge sites are likely to boost the generation of formic acid with high selectivity and activity. Heteroatom doping, such as sulfur doping, is a common way to improve catalyst performance.[14] Thermodynamically, the S atoms tend to bind to the edge sites of metallic catalysts, and the presence of S will alter the electronic structure of the adjacent sites, potentially enhancing the catalytic activity of the metal.[15] In addition, the binding of S to the edge sites of metal occupies the adsorption sites of *H, leading to suppressed HER, the major competitive reaction for

[*] L. Lv,[+] J. Zhu,[+] R. Yu, Dr. W. Zhang, E. Cui, X. Chen, Y. Dai, L. Cui, Prof. L. Zhou, Prof. W. Chen, Prof. L. Mai
State Key Laboratory of Advanced Technology for Materials Synthesis and Processing, Wuhan University of Technology
430070 Wuhan, Hubei, (P. R. China)
E-mail: mlq518@whut.edu.cn

R. Lu,[+] Dr. Z. Wang
School of Chemical Sciences, The University of Auckland
1010 Auckland (New Zealand)

Dr. J. Li
Shanghai Synchrotron Radiation Facility, Shanghai Advanced Research Institute, Chinese Academy of Sciences
201210 Shanghai (P. R. China)

Prof. L. Zhou, Prof. L. Mai
Hubei Longzhong Laboratory, Wuhan University of Technology (Xiangyang Demonstration Zone)
441000 Xiangyang, Hubei (P. R. China)

[+] These authors contributed equally to this work.

ECO_2RR.[16] Therefore, the introduction of S to the edge sites of metal may be an effective means to selectively improve the ECO_2RR performance.

Herein, we design Bi nanosheets with the edge defect sites coordinated with S via electrochemical reconstruction of $Bi_{19}Br_3S_{27}$ nanowires (BBS). The edge-sulfur- modulated bismuth catalyst demonstrates enhanced formate production and suppressed hydrogen evolution. During the structural transformation, the BBS pre-catalyst is converted into metallic Bi with abundant defects, and the Br atoms entirely escape in the form of HBr. Sulfur atoms can be partially maintained and stabilized at Bi defects' edge sites. According to theoretical calculations and electron microscopy characterization, the sulfur atoms tend to exist at the edge region of defects, which lowers the density of coordination-unsaturated Bi sites for *H adsorption whilst tailors the *p*-band center adjacent Bi sites for better ECO_2RR performance. Under alkaline conditions, the S stabilized defect-rich Bi nanosheets exhibit high formic acid Faraday efficiency ($\approx$95 %), low hydrogen Faraday efficiency ($<$5 %), and high formic acid current density ($\approx$250 mA cm^{-2}).

Results and Discussion

The BBS pre-catalyst was synthesized from a typical solvothermal reaction.[17] The X-ray diffraction (XRD) pattern of the BBS pre-catalyst shows that it consists of pure phase $Bi_{19}Br_3S_{27}$ without other diffraction peaks (Figure S1). Microscopy characterizations reveal that the BBS catalyst comprises nanowires with a smooth surface and a diameter of 100 nm, as shown in Figure S2. The X-ray energy dispersive spectroscopy (EDS) mappings of Bi, Br, and S elements clearly show their even distribution in the BBS pre-catalyst (Figure S3).

The ECO_2RR performance of BBS was evaluated in a flowing electrolytic cell with a 1.0 M KOH electrolyte, and constant CO_2 was delivered to the gas diffusion layer (Figure S4).[18] Sputtered Bi powder was synthesized as a control sample (Figure S5). Both electrodes were first activated by cyclic voltammetry (CV) scanning in the potential range of 0–−2.0 V versus reversible hydrogen electrode (RHE, all the potentials mentioned later are versus RHE unless otherwise stated). As shown in the linear scan voltammogram (LSV, Figure 1a), the BBS catalyst demonstrates a high current density of 400 mA cm^{-2} at −1.3 V in the 1.0 M KOH electrolyte, compared to the Bi control with a current density of only 150 mA cm^{-2}. Furthermore, The multipotential electrochemical impedance spectroscopy (EIS) test of BBS was performed in the range of −0.7–−1.1 V (Figure S6). The impedance decreased sharply with the decrease of applied potential, indicating that the possible phase transition can greatly reduce the electrochemical impedance of the catalysts.

The ECO_2RR performance of BBS was further evaluated by analyzing the gaseous and liquid products using gas chromatography (GC) and nuclear magnetic resonance (NMR), respectively. The results show that formate is the dominant product throughout the entire potential range (Figure 1b), with CO and H_2 as minor products. This is

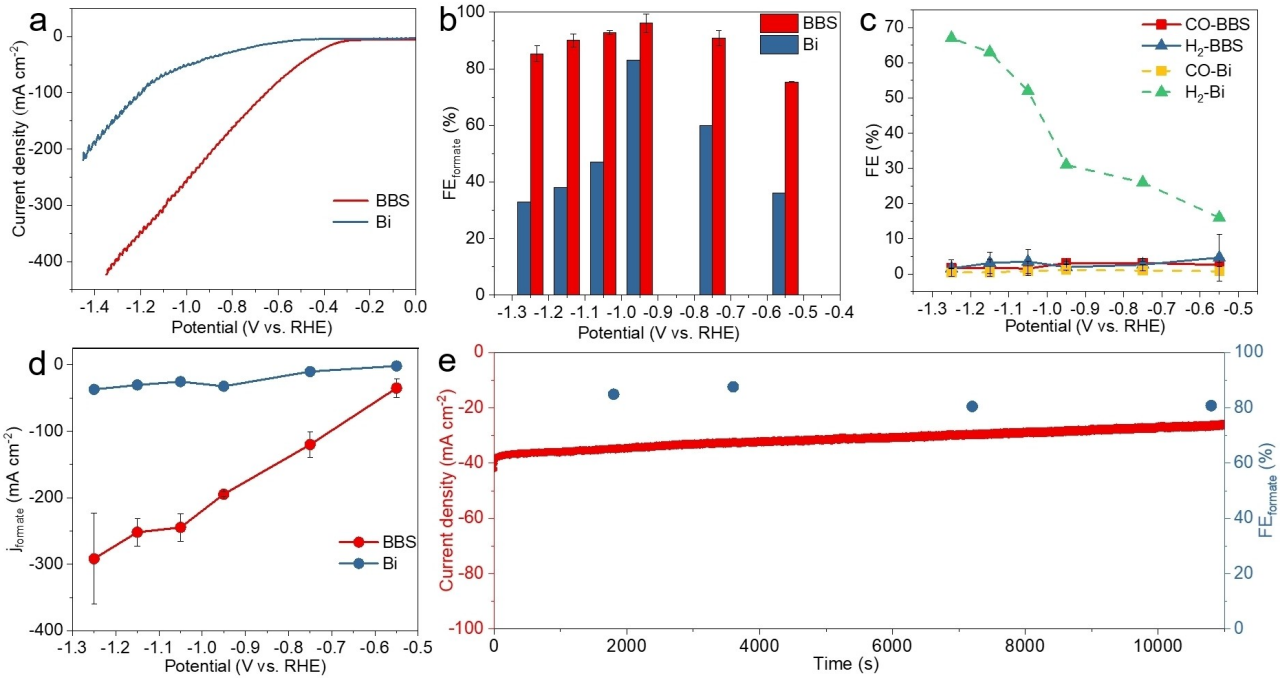

Figure 1. (a) LSV curves of BBS and Bi powder in a three-electrode flow-cell system with 1.0 M KOH electrolyte; FEs of formate (b) and H_2 and CO (c) for BBS and Bi powder in the potential range of −0.55 V–−1.25 V. (d) partial current density of formate under different applied potentials for BBS and Bi powder. (e) durability test of BBS at −0.58 V. The operating condition was as follows: anolyte and catholyte type = 1 M KOH (pH 13.9); electrolyte flow rate = 20 mL min^{-1}, average CO_2 inlet flow rate $\approx$ 50 sccm cm^{-2}; and cell temperature and pressure under atmospheric conditions.

consistent with the unfavorable adsorption of *COOH intermediates on Bi-based catalysts. The formate Faraday efficiency (FE) of BBS is more than 80 % over a wide voltage range of −0.75 to −1.25 V, with the $HCOO^-$ FE reaching 95 % at −0.95 V. In contrast, the highest formate efficiency of Bi powder in the same voltage range is only 80 %. The H_2 faraday efficiency of Bi powder is significantly higher than that of BBS (Figure 1c), indicating the effective suppression of HER on BBS. As shown in Figure 1d, the $HCOO^-$ partial current density at −0.95 V is 200 mA cm^{-2}, much higher than that of Bi powder (50 mA cm^{-2}). The ECO_2RR stability test (Figure 1e) indicates that through 10,000 s of continuous operation, BBS maintains a $HCOO^-$ FE above 80 % and a current density over 40 mA cm^{-2}, demonstrating good stability.

The change in morphology and structure of BBS after ECO_2RR may have contributed to its improved performance. The scanning electron microscopy (SEM) image of BBS after ECO_2RR shows that it has a two-dimensional nanosheet structure with abundant defects, which could enhance its surface area and increase the exposure of active sites. (Figure 2a–b and Figure S7). This transformation can be attributed to the strong reducing ability of the CO_2 reduction reaction, which leads to the escape of Br atoms and the subsequent reconstruction of the structure. Compared to the XRD pattern of the BBS before ECO_2RR (Figure S1), the XRD pattern after ECO_2RR shows the disappearance of the $Bi_{19}Br_3S_{27}$ phase and the emergence of characteristic peaks of Bi beyond the carbon paper background (Figure 2c). The three peaks marked with stars in the XRD pattern corresponds to the peaks of the carbon paper, and the XRD pattern of the blank carbon paper is shown in the supporting file (Figure S8). The partial retention of S element in the reconstructed BBS-after, as indicated by the EDS elemental mapping (Figure S9), suggests a potential role of S in stabilizing the catalyst structure during the reaction.

In situ Raman spectroscopy was employed to analyze the phase of the reconstructed BBS and accurately determine the state of Bi without interference from air exposure.[19] We performed in situ Raman characterization in a CO_2-filled 0.1 M $KHCO_3$ electrolyte (Figure 2d). As the applied potential is scanned from open circuit potential (OCP) to −1.0 V, the characteristic vibrations of BBS gradually weaken. Meanwhile, two new signals appear at 71 and 97 cm^{-1}, corresponding to the E_g and A_{1g} stretching vibrations of Bi–Bi bonds, respectively.[20] These bands illustrate the complete reconstruction of $Bi_{19}Br_3S_{27}$ nanowires to Bi nanosheets.

The evolution of the coordination environment of the reconstructed BBS catalyst under ECO_2RR conditions was studied by in situ X-ray absorption spectroscopy (XAS).[21] The Bi L_3-edge X-ray absorption near edge structure (XANES) spectra of the BBS catalyst and the same sample

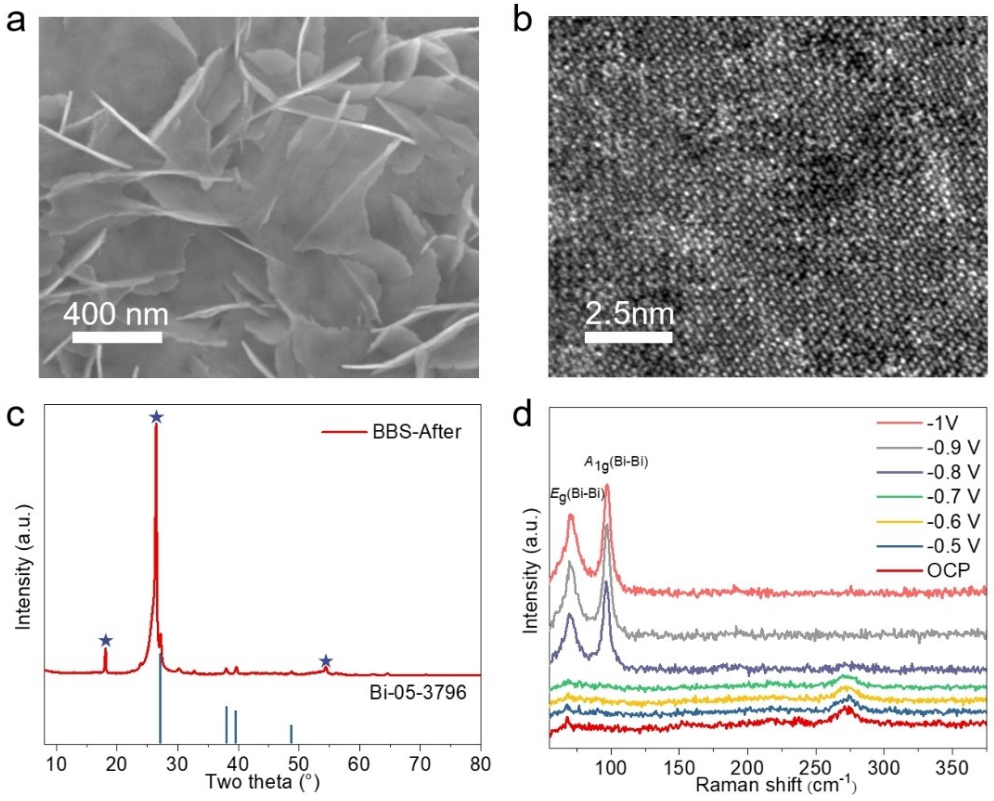

Figure 2. (a) SEM image, (b) HRTEM image, and (c) XRD pattern of the BBS catalyst after chronoamperometry test. The chronoamperometry test was as follows: the electrolyte is CO_2-filled 0.5 M $KHCO_3$, potential is −1.3 V and 5 h. (d) in situ Raman spectra of BBS in CO_2-filled 0.1 M $KHCO_3$ electrolyte.

under ECO_2RR condition at different potentials were obtained and compared with Bi foil and Bi_2O_3 as references (Figure 3a). The spectrum of BBS catalyst at OCP shows an absorption edge similar to that of BBS. At −0.95 V, the absorption edge of the reconstructed BBS is similar to Bi foil, indicating the complete reduction of BBS to metallic Bi.

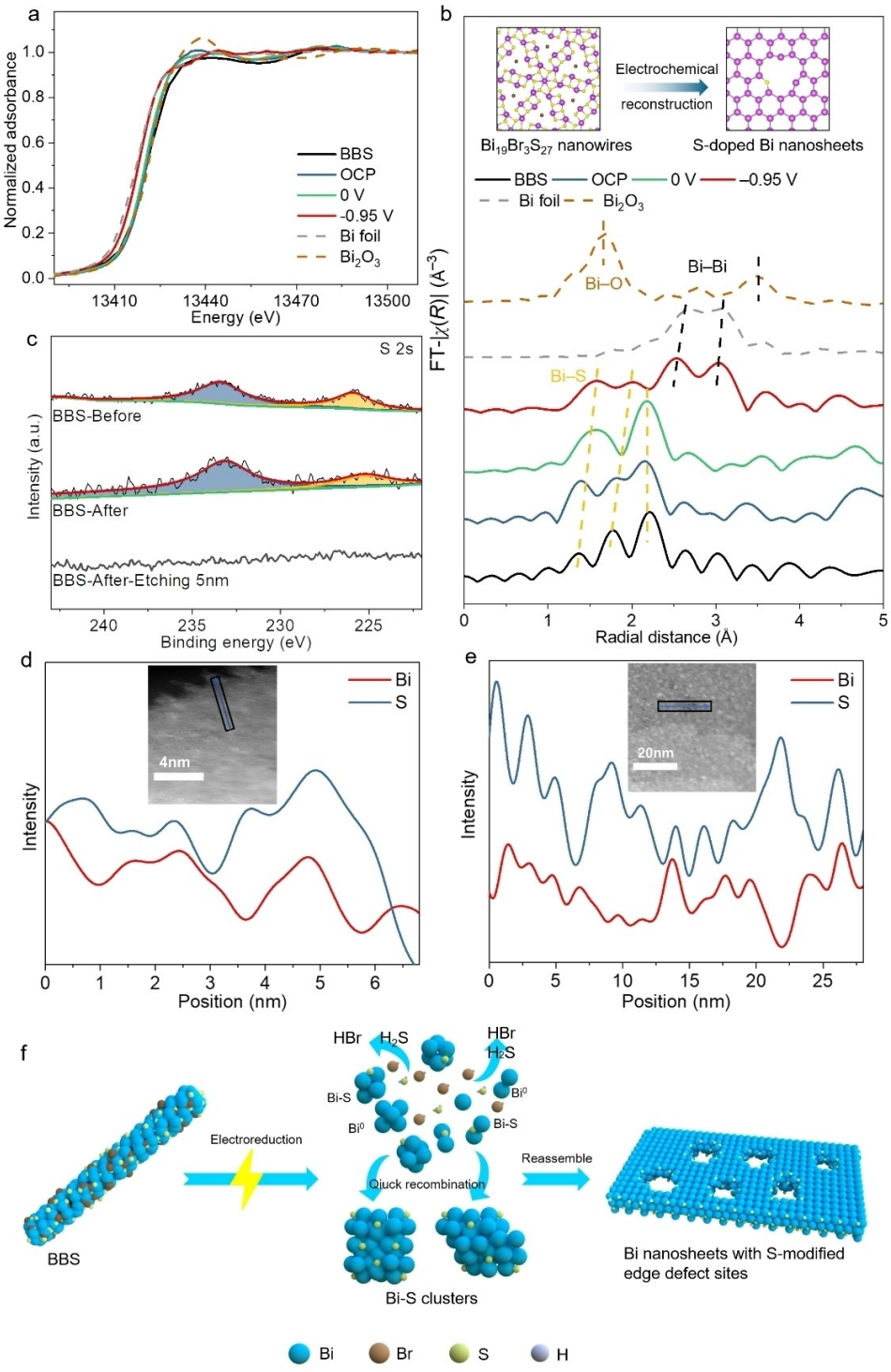

Figure 3. Normalized XANES (a), and FT $k_3\chi(R)$ EXAFS (b) of Bi L_3-edge EXAFS signals for BBS, BBS under 0 V vs. RHE, BBS under −0.95 V vs. RHE, Bi foil, and Bi_2O_3. The in situ XAFS tests are conducted in a customized three-electrode cell with CO_2-filled 0.5 M $KHCO_3$. (c) Ex situ S 2*s* XPS spectra of original BSS, BBS after chronoamperometry test and etching 5 nm. The chronoamperometry test was as follows: the electrolyte is 1.0 M KOH, potential is −0.97 V and 5 h. (d, e) EDS elemental distribution from line-scan of BBS after chronoamperometry test. The inset is HRTEM imge of BBS nanosheet edge (d) and defect (e). (f) Schematic diagram of the structural evolution from BBS to Bi nanosheets with S-modified edge defect sites.

The coordination environment of the catalyst was further analyzed by Fourier transformation of the extended X-ray absorption fine-structure (EXAFS) spectra (Figure 3b). The signals of Bi–S in BBS powder and at OCP are similar. However, at 0 V, the signals of Bi–S are disturbed due to the detachment of some S units. At the optimal potential for formate selectivity (−0.95 V), the Bi–Bi coordination signal is strongly expressed, consistent with the in situ Raman results, but the Bi–S coordination signal still remains. Furthermore, the intensity of the Bi–S coordination signal becomes weaker at −0.95 V, indicating that most S atoms leave the electrode during the reduction process, while a small fraction remains in the form of Bi–S bonds on the electrode surface. The in situ XAS results provide insights into the coordination environment of the BBS catalyst during ECO_2RR and the changes in the catalyst structure.

Ex situ XPS was performed on the BBS catalyst (Figure S10) to confirm its phase composition further. The S 2*s* spectra (Figure 3c) show that the S element does exist in BBS after the reaction. Ar^+ etching was performed, and the S signal was found to be absent after 5 nm, indicating that the S content is low and mainly present on the surface of the catalyst. Taking into account the potential degradation of S in alkaline solutions, we collected S 2*s* XPS spectra of BBS after conducting a chronoamperometry test in 0.5 M $KHCO_3$. Figure S11 illustrates that the remaining quantity of S did not vary between neutral and alkaline solutions, indicating that the S component in BBS is not subject to deterioration in an alkaline electrolyte solution. Moreover, the Bi 4*f* XPS spetra of BBS after ECO_2RR treatment shows a positive valence state due to partial oxidation of Bi sites and binding to S (Figure S12). After etching, Bi^0 was observed because S units mainly exist on the catalyst's surface. The Br 3*d* spectra (Figure S13) show Br escapes completely after the ECO_2RR.

To visualize the distribution of S in Bi nanosheets derived from BBS, high-angle annular dark-field scanning transmission electron microscopy (HAADF-STEM) was used. As shown in Figure 3d, and e, there are numerous nanopores on the nanosheets, which are formed due to the escape of Br and S and the rapid reassembly of Bi atoms. The EDS line scan (Figure 3d) reveals that the S content at the edges of the nanosheets is higher than that in bulk regions. In addition, Figure 3e indicates that the S content is significantly higher around the nanosheet defects. These results suggest that during the ECO_2RR process, some S atoms escape from the electrode, and the remaining S atoms are mainly present at the edge region on the catalyst surface. It is our belief that the reduction and reconstruction process of BBS nanowires implicated the diffusion and deposition of Bi atoms/clusters, with the release of H_2S and HBr promoting the formation of defect sites (Figure 3f). Additionally, the residual S component exhibited a tendency to remain at the edge.

In situ attenuated total reflection surface-enhanced infrared adsorption spectroscopy (ATR-SERIES) is an effective technique to monitor the evolution of reaction intermediates.[22] We implemented in situ ATR-SERIES in a 0.1 M $KHCO_3$ electrolyte with a constant flux of CO_2 and in a potential range of 0.01 V–−1.39 V (Figure S14). As shown in Figure S15, the two enhancement bands observed at 1339 and 1646 cm^{-1} were attributed to symmetric and asymmetric stretching vibrations of the COO radical, respectively. The wave-number difference between the two bands suggests that the COO radical is bound to the metal site through a monodentate configuration.[23] The bending vibration of COO in the plane at 1361 cm^{-1} is the vibration of the COOH radical.[10c,24] Therefore the conversion to formic acid via *OCHO intermediate is the reaction path for BBS-catalyzed CO_2 reduction, which is also the optimal path for the formate formation.

Further analysis of the calculated adsorption energy and reaction pathways using first-principle density functional theory (DFT) shows that the S atoms at the edge of the Bi nanosheets play a crucial role in facilitating the CO_2 reduction reaction. As displayed in Figure 4a, five possible catalytic sites were considered, namely, pure Bi, S–Bi (the S is bonded with three Bi atoms), V–Bi (Bi with defects), S, V(S)–Bi (the S is bonded with three Bi atoms in defect-containing Bi), and S, V(Bi)–Bi (the S is bonded to the edge defects of Bi). On these sites, we calculated the corresponding free energy changes of the $2e^-$ ECO_2RR process towards HCOOH (Figure 4b). The step with the highest energy increase is the rate-determining step. Figure 4b shows that the pure Bi site has weak *OCHO adsorption, leading to a high overpotential of 1.23 V for ECO_2RR to HCOOH. On the other hand, the S–Bi site strongly binds with *OCHO, resulting in a significantly lower overpotential of 0.23 V. The presence of Bi vacancy on V–Bi exposed Bi sites further enhances *OCHO adsorption, leading to a further decrease in the overpotential to 0.02 V. Compared to the pure Bi, the S, V(S)–Bi and S, V(Bi)–Bi show better catalytic activity, with overpotentials of 0.01 and 0.06 V, respectively. Overall, V–Bi, S, V(S)–Bi, and S, V(Bi)–Bi are the main active sites for catalyzing CO_2 into HCOOH.

During electrochemical CO_2 reduction, HER is a competitive catalytic reaction and CO is another ECO_2RR production, both of which can lower the formate selectivity. The selectivity towards H_2 and CO is determined by the adsorption energies of *H and *COOH, respectively. In Figure 4c, it is shown that although all V–Bi, S, V(S)–Bi, and S, V(Bi)–Bi sites have suitable adsorption energy towards *OCHO, V–Bi has good *COOH adsorption energy, and S, V(Bi)–Bi shows good selectivity towards *H and *COOH. Only S, V(S)–Bi inhibits *H and *COOH adsorption, which is favorable for formate selectivity.

The effect of S modulation on the electronic structure was investigated through further calculations. The charge density difference in the inset of Figure 4d shows electron transfers from neighboring Bi to the S atom, indicating the electron-withdrawing capacity of S. Figure 4d demonstrates a strong correlation between Bi *p*-band center and *OCHO adsorption energy, indicating the effect of S configuration on the electronic structure. The number of edge S configurations largely affected the density of active S, V(S)–Bi. Formation energies of V–Bi, S, V(S)–Bi, S, V(Bi)–Bi, and pure Bi were compared in Figure 4e, and it was found that the edge double-bonded S species could stabilize the Bi

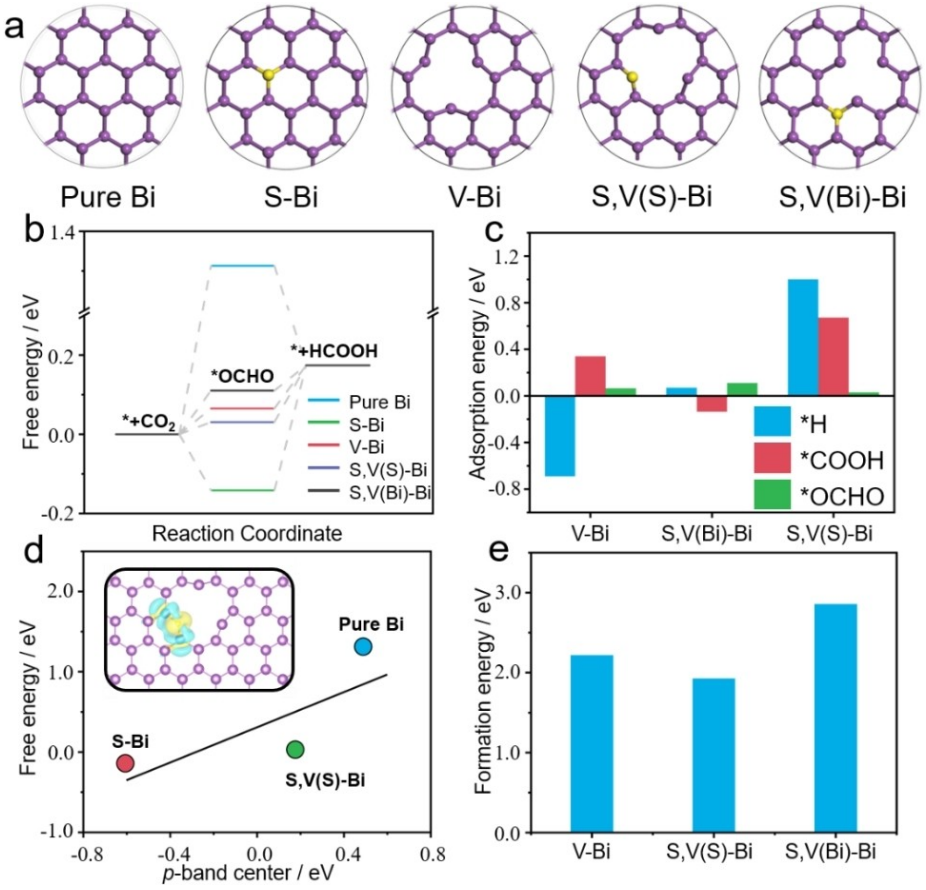

Figure 4. (a) The top view of pure Bi, S–Bi, V–Bi, S, V(S)–Bi, and S, V(Bi)–Bi catalysts. The yellow and purple balls represent S and Bi atoms, respectively. (b) The free energy profile along CO_2RR on catalytic sites. (c) The *H (ΔG_{*H}), *COOH (ΔG_{*COOH}), and *OCHO (ΔG_{*OCHO}) adsorption energy on V–Bi, S, V(S)–Bi, and S, V(Bi)–Bi catalysts. (d) The correlation between adsorption energy (ΔG_{*OCHO}) and *p*-band center of active Bi atoms. The inset is the charge density difference. The yellow and blue areas denote electronic accumulation and depletion, respectively. (e) The formation energies of V–Bi, S, V(S)–Bi, and S, V(Bi)–Bi.

vacancy and exhibited a lower formation energy compared to V–Bi and S, V(Bi)–Bi, making S dopant favorable for locating at the edge defects of bismuth. Moreover, increasing the edge S configurations further improved the stability of Bi catalysts (Figure S16) and greatly promoted ECO_2RR activity. In summary, binding S to the edge sites of Bi selectively inhibits HER while ensuring strong *OCHO adsorption.

Conclusion

In conclusion, Bi nanosheets with S-modified edge defect sites are synthesized via electrochemical reconstruction of $Bi_{19}Br_3S_{27}$ nanowires. In situ and ex situ characterizations reveal that the S dopants are mainly located at the edge sites of the Bi nanosheets, which exhibit strong adsorption ability to *OCHO intermediates and can inhibit the production of H_2 and CO intermediates during ECO_2RR. In an alkaline electrolyte, the resulting edge-sulfur modulated Bi nanosheets exhibit high current density ($\approx$400 mA cm^{-2}) and FE of $HCOO^-$ (>90 %) and very low FE of H_2 (<5 %) over a wide potential range. This work highlights the importance of precise coordination structure adjustment for the development of highly efficient ECO_2RR electrocatalysts.

Acknowledgements

This work was supported by the National Key Research and Development Program of China (2020YFA0715000), National Natural Science Foundation of China (52127816, 51832004), Independent Innovation Project of Hubei Longzhong Laboratory (2022ZZ-18), State Key Laboratory of Advanced Technology for Materials Synthesis and Processing (2021-KF-23). We thank Beamline BL11B at SSRF for the XAFS measurement. The computational study is supported by the Marsden Fund Council from Government funding (21-UOA-237) and Catalyst: Seeding General Grant (22-UOA-031-CGS), managed by Royal Society Te Apārangi. ZW and RL wish to acknowledge the use of New Zealand eScience Infrastructure (NeSI) high-performance computing facilities, consulting support and/or training services as part of this research.

Conflict of Interest

The authors declare no conflict of interest.

Data Availability Statement

The data that support the findings of this study are available from the corresponding author upon reasonable request.

Keywords: Carbon Dioxide Reduction · Electrocatalysis · Electrochemical Reconstruction · S-Doping

[1] a) G. Wang, J. Chen, Y. Ding, P. Cai, L. Yi, Y. Li, C. Tu, Y. Hou, Z. Wen, L. Dai, *Chem. Soc. Rev.* **2021**, *50*, 4993–5061; b) S. Verma, S. Lu, P. J. A. Kenis, *Nat. Energy* **2019**, *4*, 466–474; c) Y. Quan, J. Zhu, G. Zheng, *Small Sci.* **2021**, *1*, 2100043.

[2] a) Z. Zeng, L. Y. Gan, H. Bin Yang, X. Su, J. Gao, W. Liu, H. Matsumoto, J. Gong, J. Zhang, W. Cai, Z. Zhang, Y. Yan, B. Liu, P. Chen, *Nat. Commun.* **2021**, *12*, 4088; b) Y. Wu, W. Wei, R. Yu, L. Xia, X. Hong, J. Zhu, J. Li, L. Lv, W. Chen, Y. Zhao, L. Zhou, L. Mai, *Adv. Funct. Mater.* **2022**, *32*, 2110910; c) L. Zhang, J. Zhu, X. Li, S. Mu, F. Verpoort, J. Xue, Z. Kou, J. Wang, *Interdiscip. Mater.* **2022**, *1*, 51–87.

[3] X. Liu, C. Xing, F. Yang, Z. Liu, Y. Wang, T. Dong, L. Zhao, H. Liu, W. Zhou, *Adv. Energy Mater.* **2022**, *12*, 2201009.

[4] a) R. Lincoln, M. L. Bossi, M. Remmel, E. D'Este, A. N. Butkevich, S. W. Hell, *Nat. Chem.* **2022**, *14*, 1013; b) S. Cheng, Z. Sun, K. H. Lim, T. Z. H. Gani, T. Zhang, Y. Wang, H. Yin, K. Liu, H. Guo, T. Du, L. Liu, G. K. Li, Z. Yin, S. Kawi, *Adv. Energy Mater.* **2022**, *12*, 2200389; c) Z. Zhang, M. Wang, Z. Chi, W. Li, H. Yu, N. Yang, H. Yu, *Appl. Catal. B* **2022**, *313*, 121426; d) R. Paul, Q. Zhai, A. K. Roy, L. Dai, *Interdiscip. Mater.* **2022**, *1*, 28–50.

[5] K. Guo, X. Li, H. Lei, H. Guo, X. Jin, X. P. Zhang, W. Zhang, U. P. Apfel, R. Cao, *Angew. Chem. Int. Ed.* **2022**, *61*, e202209602.

[6] a) Z. Sun, T. Ma, H. Tao, Q. Fan, B. Han, *Chem* **2017**, *3*, 560–587; b) M. B. Ross, P. De Luna, Y. Li, C.-T. Dinh, D. Kim, P. Yang, E. H. Sargent, *Nat. Catal.* **2019**, *2*, 648–658; c) R. I. Masel, Z. Liu, H. Yang, J. J. Kaczur, D. Carrillo, S. Ren, D. Salvatore, C. P. Berlinguette, *Nat. Nanotechnol.* **2021**, *16*, 118–128.

[7] a) P. De Luna, C. Hahn, D. Higgins, S. A. Jaffer, T. F. Jaramillo, E. H. Sargent, *Science* **2019**, *364*, eaav3506; b) Z. Zhang, S. Chen, J. Zhu, C. Ye, Y. Mao, B. Wang, G. Zhou, L. Mai, Z. Wang, X. Liu, D. Wang, *Nano Lett.* **2023**, *23*, 2312–2320.

[8] a) O. S. Bushuyev, P. De Luna, C. T. Dinh, L. Tao, G. Saur, J. van de Lagemaat, S. O. Kelley, E. H. Sargent, *Joule* **2018**, *2*, 825–832; b) Z. Zhuang, L. Xia, J. Huang, P. Zhu, Y. Li, C. Ye, M. Xia, R. Yu, Z. Lang, J. Zhu, L. Zheng, Y. Wang, T. Zhai, Y. Zhao, S. Wei, J. Li, D. Wang, Y. Li, *Angew. Chem. Int. Ed.* **2023**, *62*, e202212335.

[9] W. Zhang, S. Yang, M. Jiang, Y. Hu, C. Hu, X. Zhang, Z. Jin, *Nano Lett.* **2021**, *21*, 2650–2657.

[10] a) E. Zhang, T. Wang, K. Yu, J. Liu, W. Chen, A. Li, H. Rong, R. Lin, S. Ji, X. Zheng, Y. Wang, L. Zheng, C. Chen, D. Wang, J. Zhang, Y. Li, *J. Am. Chem. Soc.* **2019**, *141*, 16569–16573; b) M. Zhang, W. Wei, S. Zhou, D.-D. Ma, A. Cao, X.-T. Wu, Q.-L. Zhu, *Energy Environ. Sci.* **2021**, *14*, 4998–5008; c) W. Zhang, C. Huang, Q. Xiao, L. Yu, L. Shuai, P. An, J. Zhang, M. Qiu, Z. Ren, Y. Yu, *J. Am. Chem. Soc.* **2020**, *142*, 11417–11427.

[11] Q. Gong, P. Ding, M. Xu, X. Zhu, M. Wang, J. Deng, Q. Ma, N. Han, Y. Zhu, J. Lu, Z. Feng, Y. Li, W. Zhou, Y. Li, *Nat. Commun.* **2019**, *10*, 2807.

[12] D. Yao, C. Tang, A. Vasileff, X. Zhi, Y. Jiao, S. Z. Qiao, *Angew. Chem. Int. Ed.* **2021**, *60*, 18178–18184.

[13] Y. Shen, H. Yu, T. Xu, Q. Zhang, K. Yin, S. Cong, Y. Liu, L. Sun, *Nano Res.* **2022**, *15*, 4710–4716.

[14] a) P. Deng, H. Wang, R. Qi, J. Zhu, S. Chen, F. Yang, L. Zhou, K. Qi, H. Liu, B. Y. Xia, *ACS Catal.* **2020**, *10*, 743–750; b) M. Al-Mamun, Z. Zhu, H. Yin, X. Su, H. Zhang, P. Liu, H. Yang, D. Wang, Z. Tang, Y. Wang, H. Zhao, *Chem. Commun.* **2016**, *52*, 9450–9453.

[15] a) R. Li, F. Liu, Y. Zhang, M. Guo, D. Liu, *ACS Appl. Mater. Interfaces* **2020**, *12*, 44578–44587; b) W. Zhou, H. Yang, N. Gao, D. Zhang, Z. Li, F. Gao, C. Nan, *J. Alloys Compd.* **2022**, *903*, 163707.

[16] a) Y. C. Wang, Y. J. Lai, L. Song, Z. Y. Zhou, J. G. Liu, Q. Wang, X. D. Yang, C. Chen, W. Shi, Y. P. Zheng, M. Rauf, S. G. Sun, *Angew. Chem. Int. Ed.* **2015**, *54*, 9907–9910; b) S. S. Shinde, A. Sami, D. H. Kim, J. H. Lee, *Chem. Commun.* **2015**, *51*, 15716–15719.

[17] J. Li, W. Pan, Q. Liu, Z. Chen, Z. Chen, X. Feng, H. Chen, *J. Am. Chem. Soc.* **2021**, *143*, 6551–6559.

[18] E. W. Lees, B. A. W. Mowbray, F. G. L. Parlane, C. P. Berlinguette, *Nat. Rev. Mater.* **2022**, *7*, 55–64.

[19] Q. Zhou, W. Zhang, M. Qiu, Y. Yu, *Mater. Today Phys.* **2021**, *20*, 100443.

[20] a) J. Zhu, S. Li, Z. Zhuang, S. Gao, X. Hong, X. Pan, R. Yu, L. Zhou, L. V. Moskaleva, L. Mai, *Energy Environ. Mater.* **2022**, *5*, 231–237; b) J. Wei, S. N. Qin, J. L. Liu, X. Y. Ruan, Z. Guan, H. Yan, D. Y. Wei, H. Zhang, J. Cheng, H. Xu, Z. Q. Tian, J. F. Li, *Angew. Chem. Int. Ed.* **2020**, *59*, 10343–10347.

[21] a) J. Zhu, L. Xia, W. Yang, R. Yu, W. Zhang, W. Luo, Y. Dai, W. Wei, L. Zhou, Y. Zhao, L. Mai, *Energy Environ. Mater.* **2022**, *5*, 655–661; b) W. Zhang, C. Huang, J. Zhu, Q. Zhou, R. Yu, Y. Wang, P. An, J. Zhang, M. Qiu, L. Zhou, L. Mai, Z. Yi, Y. Yu, *Angew. Chem. Int. Ed.* **2022**, *61*, e202112116.

[22] a) N. J. Firet, W. A. Smith, *ACS Catal.* **2017**, *7*, 606–612; b) S. Chen, A. Chen, *J. Phys. Chem. C* **2019**, *123*, 23898–23906; c) A. D. Handoko, F. Wei, Jenndy, B. S. Yeo, Z. W. Seh, *Nat. Catal.* **2018**, *1*, 922–934.

[23] a) S. Zhu, T. Li, W.-B. Cai, M. Shao, *ACS Energy Lett.* **2019**, *4*, 682–689; b) M. Huang, S. Gong, C. Wang, Y. Yang, P. Jiang, P. Wang, L. Hu, Q. Chen, *Angew. Chem. Int. Ed.* **2021**, *60*, 23002–23009; c) S. Chen, Z. Zhang, W. Jiang, S. Zhang, J. Zhu, L. Wang, H. Ou, S. Zaman, L. Tan, P. Zhu, E. Zhang, P. Jiang, Y. Su, D. Wang, Y. Li, *J. Am. Chem. Soc.* **2022**, *144*, 12807–12815.

[24] a) S. Zhu, B. Jiang, W. B. Cai, M. Shao, *J. Am. Chem. Soc.* **2017**, *139*, 15664–15667; b) Y. Kim, S. Park, S.-J. Shin, W. Choi, B. K. Min, H. Kim, W. Kim, Y. J. Hwang, *Energy Environ. Sci.* **2020**, *13*, 4301–4311.

Manuscript received: March 1, 2023
Accepted manuscript online: April 20, 2023
Version of record online: ■■, ■■

Research Articles

CO_2 Reduction

L. Lv, R. Lu, J. Zhu, R. Yu, W. Zhang, E. Cui, X. Chen, Y. Dai, L. Cui, J. Li, L. Zhou, W. Chen, Z. Wang, L. Mai* — **e202303117**

Coordinating the Edge Defects of Bismuth with Sulfur for Enhanced CO_2 Electroreduction to Formate

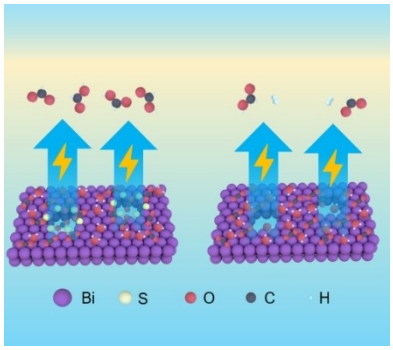

The Bi nanosheets with the edge defect sites coordinated with S via electrochemical reconstruction of $Bi_{19}Br_3S_{27}$ nanowires (BBS), and the edge-sulfur modulated Bi catalyst demonstrates enhanced formate production and suppressed hydrogen evolution. In an alkaline electrolyte, the edge-sulfur modulated Bi nanosheets exhibit high current density ($\approx$400 mA cm^{-2}) and FE of $HCOO^-$ ($>$90%) and very low FE of H_2 ($<$5%) over a wide potential range.